CHARACTERIZING THERMAL EXPANSION OF LARGE-SCALE 3D PRINTED PARTS

Dylan Hoskins[1], Vlastimil Kunc[1,2], Ahmed Hassen[2], John Lindahl[2], Chad Duty[1,2]

[1]University of Tennessee Knoxville
1512 Middle Dr
Knoxville, TN 37916

[2] Manufacturing Demonstration Facility, Oak Ridge National Laboratory
2360 Cherahala Blvd
Knoxville, TN 37932

ABSTRACT

Additively manufactured parts have an inherent mesostructure as a result of printing artifacts. The build structure is defined by parameters such as infill pattern, raster spacing, and bead height, and can impart anisotropic thermo-mechanical properties that are different from the bulk properties of the feedstock. The anisotropy is more pronounced when printing with fiber reinforced polymers due to the shear-alignment of fibers during the extrusion process. This study evaluates the combined effects of the printed mesostructure and the fiber-aligned microstructure on the coefficient of thermal expansion of large-scale printed parts. A digital image correlation-based method for recording thermal strain across the surface of a printed part is described. Measured values are compared to predictions based on laminate theory using the anisotropic material properties at the microscale for common raster orientations.

1. INTRODUCTION

1.1 Thermal Expansion of Additively Manufactured Parts

Extrusion deposition additive manufacturing (EDAM) allows the rapid creation of parts with complex geometries using systems ranging from a desktop fused filament fabrication (FFF) printer to large-area extrusion deposition machines, including the Manufacturing Demonstration Facility's (MDF) Big Area Additive Manufacturing (BAAM) system. There are opportunities for implementation of AM in the aerospace, dental, and medical fields [1-3]. One opportunity of significant interest is the manufacturing of tooling for composites, which commonly have complex geometries and long lead times. Previous works on the practicality of state-of-the-art technologies have shown the use of additive manufacturing (AM) processes can reduce lead time and cost of manufacturing tooling [4-8]. Some tooling, such as those used in autoclaves, can undergo temperature change during the production of the composites. This means the thermomechanical behavior of the tooling are important, for if the linear coefficients of thermal

SAMPE Conference Proceedings. Charlotte, NC, May 20-23, 2019. Society for the Advancement of Material and Process Engineering – North America.

expansion (LCTE) of the tooling and the composite being produced from the tooling are mismatched, then the composite will have distortion that could render the part unusable [9]. Parts manufactured using FFF or EDAM are created by depositing beads of material into the desired shape to create one layer in the x-y plane, raising the extruding nozzle, and depositing another layer on top of the previous one. The path the nozzle takes to deposit the beads to make these layers is referred to as the toolpath. The toolpath for an AM part comes in many forms: rectilinear, concentric, honeycomb and many others. The combination of all the beads in each layer create the macrostructure of the part. The macrostructure determines the thermomechanical properties of the part as a whole, as it defines the amount of bulk material and bead to bead interfaces being strained. Cited works have documented anisotropy due to macrostructure [10-13]. The anisotropy from the macrostructure is heightened when the feedstock for the part is a carbon fiber reinforced polymer, which is critical in large area extrusion deposition additive manufacturing (LAEDAM), such as the BAAM, for reducing distortion [14, 15]. Anisotropy increases due to the stiffness of the fibers embedded in the matrix material. The fiber-matrix interface allows thermal and mechanical stresses to be transferred from the matrix to the fibers [16]. Therefore, the amount of stress that can be transferred to a fiber in a direction will affect mechanical and thermomechanical properties. The amount of transferrable stress determines the composite's properties and will be a function of aspect ratio, fiber orientation and the fiber-matrix interface [17, 18]. During printing, fibers primarily align in the print direction of the bead, which is due to the shear forces experienced by the material during extrusion [19, 20]. Although the majority of the fibers align in the print direction, fiber orientation does vary throughout a bead. Fibers are more oriented in the print direction near the outside perimeter of the bead and more randomly oriented towards the center , leading to anisotropy within the bead itself [21]. Therefore, a part produced using LAEDAM will have anisotropy from both micro- and macro-scale features, and as fibers align with print direction, which is part of the macrostructure, the two become intertwined [20]. The part having anisotropy on the macroscale results in the traditional LCTE testing standard, ASTM E831-14, which is intended for a sample of less than ten millimeters in any direction, to be a poor estimate of the part as a whole, even if it is accurate for measuring LCTE of the beads that form the macrostructure [22]. This study explores the use of digital image correlation (DIC) for measuring the LCTE of large-scale printed parts in various directions and compares results against both conventional thermomechanical analysis (TMA) of small-scale samples and theoretical predictions using composite laminate theory.

2. EXPERIMENTATION

2.1 Materials

Three samples were created to be used in this work. They were printed on the BAAM system at MDF. The samples were printed from 20% carbon fiber by weight in a matrix of acrylonitrile butadiene styrene (ABS) procured from Techmer PM with the trade name Electrafil J-1200/CF/20. The three samples, seen in Figure 1 (a-c) used in this work were printed with a 10.2 mm nozzle at 200 °C on the BAAM system. Two large cubes (127 mm x 127 mm x 127 mm) were printed for DIC, one with raster orientation of 0-0, meaning each layer is formed by straight beads side by side and every layer is in the same direction, and the other with a raster orientation of 0-90, where every layer is still formed by side by side beads but rotated ninety degrees from the previous layer. Both cubes were machined flat on all six faces of the cube. The third sample was a smaller cube (50 mm x 50 mm x 50 mm) printed with 0-0 raster orientation for machining into TMA samples (10 mm x 3 mm x 4mm). For the DIC measurements, the two large cubes were painted white on the faces of interest using high-temperature spray paint and then speckled with black ink using a rubber stamp, with a dot sizing of .18mm, and multiple passes at different angles**.** Figure 1 (b), for reference, is representative of a cube specimen, speckled and ready for DIC.

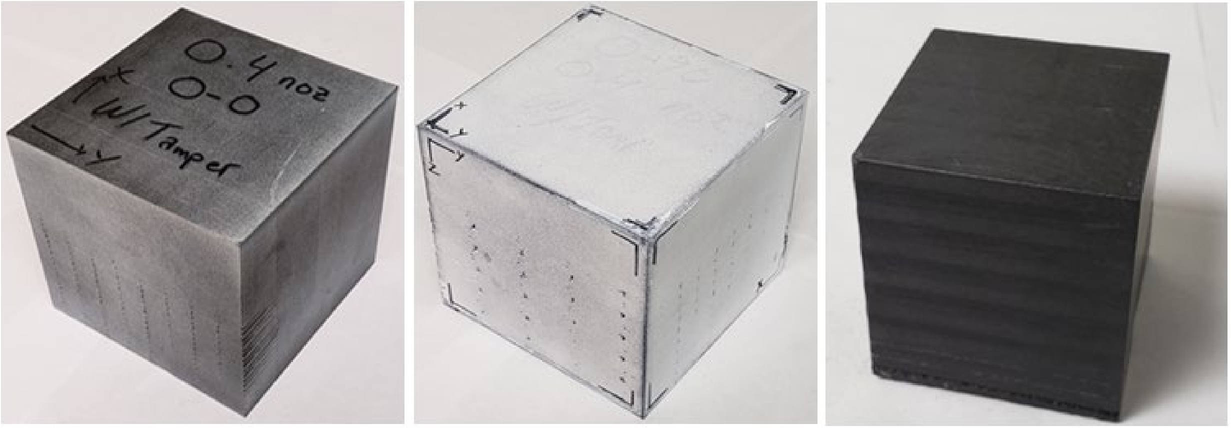

Figure 1. Images of the samples used in this work (a) 127 mm 0-0 cube, (b) 127 mm 0-90 cube after DIC preparation (speckling), (c) 50 mm 0-0 cube for TMA samples

2.2 DIC Setup and Imaging

DIC is an optical method of measuring in plane deformations of an object [23]. The setup used for the present work is a specially-designed oven with a temperature control system from Applied Testing Systems. The oven has single paned viewports in the bottom and one side of the oven to allow for DIC imaging. The five-megapixel camera (Correlated Solutions CSI-5MP) is positioned underneath the bottom viewport to take images of the bottom horizontal plane of the sample, which rests over a hole on a horizontal shelf (Figure 2a). The novel camera position and sample placement in this set up has two main benefits. The first benefit is that in a traditional side viewing DIC set up, there are natural convective waves moving up the sides of the cube that can cause significant noise during imaging. Capturing images from the bottom camera position will largely reduce natural convective flow around the face of interest as it is now horizontal. The second advantage over a conventional camera setup is that out of plane deformations are no longer a concern. In the standard side-view, the specimen would be able to expand out of the vertical plane where strain was being measured originally. Out of plane movement can introduce bias to the two-dimensional strain measurements, which requires a complex multi-camera system be implemented for corrections. Using the bottom camera position and sample placement, all vertical expansion will be relative to the shelf and the horizontal face of interest will not move with respect to the camera. The camera is controlled by a National instruments NI cDAQ™-9174. Inside of the oven is a shelf for sample placement, interior lighting on two opposing corners of the bottom viewport, and one lighting source on the back-interior wall. An image of the setup can be seen in Figure 2b. Vic-Snap software was used for capturing the images, and the analysis of the images for DIC was done using Vic-2D.

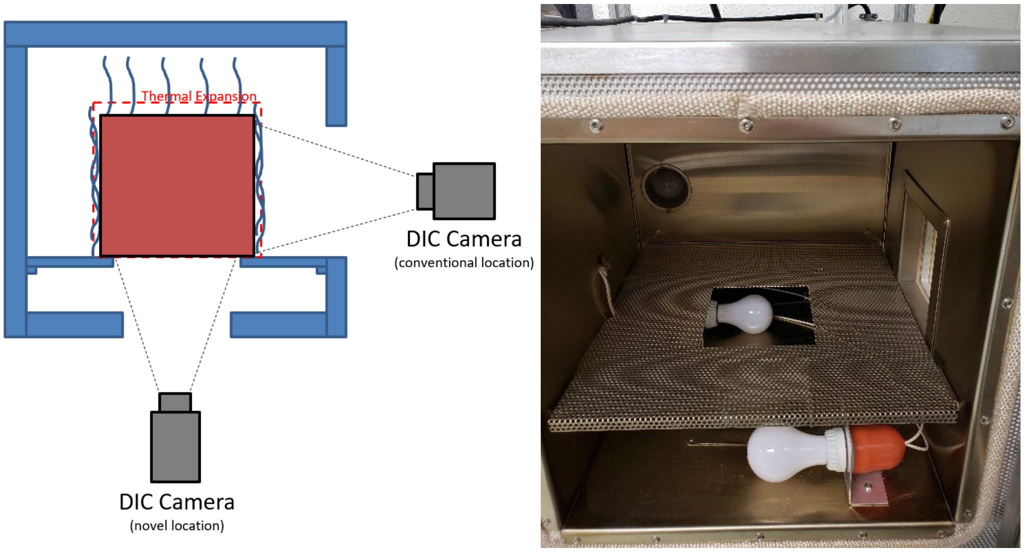

Figure 2. (a) Depiction of novel camera set up, (b) Image of oven used to heat samples

The samples were placed on the shelf above the bottom viewport with the surface of interest facing down. The cube axes were labelled with respect to their print orientation: the x-axis is the primary horizontal print direction, the y-axis is on the same horizontal plane perpendicular to the x-axis, and the z-axis is in the vertical print direction. The 0-90 cube does not have a primary horizontal print direction, the direction in which the majority of its layers align, therefore the x-axis was chosen to be the print direction of the imaged surface. Forty-five images of the sample were taken at room temperature (~20 °C) at a sampling rate of 100ms. The oven was then heated to 90 °C, and the sample was allowed to reach equilibrium by resting at 90 °C for 24 hours after which 45 more images were taken of the sample at a sampling rate of 100ms. The images were then processed with Vic-2D software. In general, DIC divides the reference image up into a grid. The sizing of this grid is referred to as the subset size and each point, P, where the grid intersects is the center of a subset. A subset size of 65 x 65 pixels was chosen based on Vic-2D's recommendation for the speckling pattern used. The gray intensity of each subset is calculated and is used track P to its location in the corresponding deformed image. The new and old position of P are then used to calculate a displacement vector. Using the displacement vector, the strain in the x- and y-axes of the camera, which will be referred to as the x'-and y'- axes from now on, is calculated [23].

Strain data in the x'- and y'-axes was collected from each cube at both 20 °C and 90 °C. Strain data from the 45 images in each direction, x' and y', was averaged at both temperatures, which creates four averaged datasets for each cube. As the sample is at 20 °C in the first forty-five photos and is being compared to a photo at 20 °C, any measured strain is simply treated as noise in the system. Thus, since it is noise (δ), it was subtracted from the 90 °C photos to give an accurate representation of the actual strain due to temperature change at 90 °C. Measured strain is divided by the change in temperature to find the coefficient of thermal expansion in the respective direction, as is shown in Equation 1.

$$LCTE_i = \frac{\epsilon_i^{High\,Temp} - \delta_i^{Low\,Temp}}{\Delta T} \qquad [1]$$

2.3 Thermomechanical Analysis

Thermomechanical analysis is a well-established method of determining the LCTE of a sample in accordance with ASTM standard E831-14, which was used a general guideline during testing. Deviations from the standard and required additional information: specimens were dried at 85 °C for 6 hours and placed inside a desiccator to cool to room temperature to ensure no moisture in the samples and only one sample from each position was tested [22]. The tests were conducted on an TA Instruments Q400EM TMA. Two samples (10 mm x 3 mm x 4 mm) were cut from a single bead of the small-scale sample using a Buehler IsoMet1000 saw. Samples were cut from the locations depicted in Figure 3 and there was a kerf of .15 mm between the two samples. Two samples were necessary because fiber orientation within a bead is not uniform, as described earlier and as seen in Figure 4. Variation in fiber orientation will affect the LCTE of the samples, so the sample locations were chosen to try to capture both the highly aligned outer shell and the less aligned core. LCTE was measured once in the x, y, and z directions for each sample between the range of 30 °C to 85 °C using TA Instruments Universal Analysis software, which finds the slope of the dimensional change versus temperature graph between the two temperatures. The average of the two values was calculated for each direction.

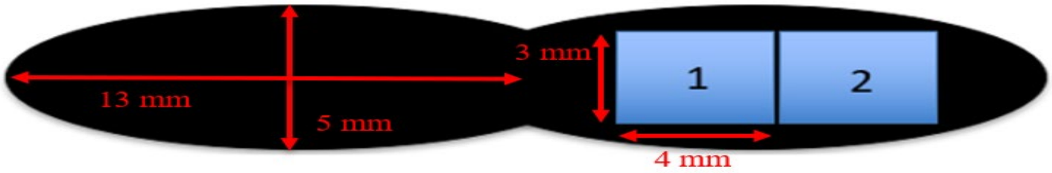

Figure 3. Depiction of TMA sample location within the printed bead

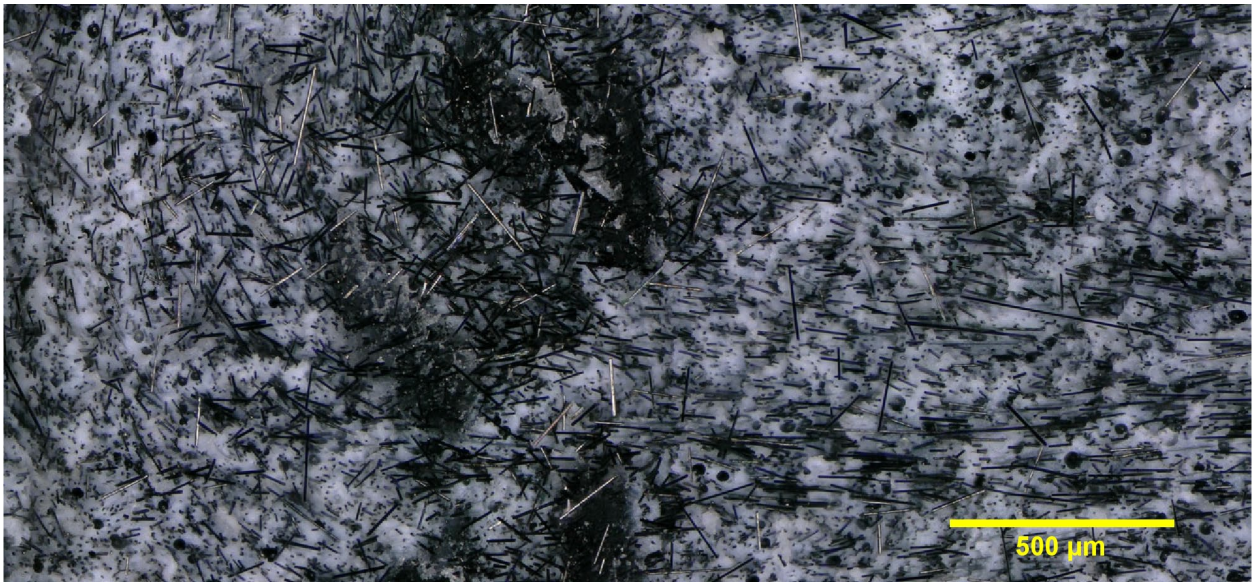

Figure 4. Micrograph of BAAM system bead showing varied fiber orientation

3. RESULTS

3.1 TMA Results

Figure 5 shows a representative graph of the thermal expansion of a small-scale sample (sample 1) in the x-direction between the temperatures of 30 °C and 85 °C. This was done for x- and y-direction in both samples, creating four datasets, and the results can be viewed in Table 1. As expected from literature and the micrograph shown earlier, the samples do show variance in the same bead. Given LCTE values of the samples, it is likely that sample 2 had high fiber orientation in the x-direction, resulting in the lower value. Large observable differences in LCTE between two samples that are so close together is an indication of how much fiber orientation can vary through a small distance within a bead. Drastic changes in such a short span exhibits the need for multiple samples across a bead to fully understand the thermomechanical behavior of an individual bead, which can then be treated representative of a typical bead. Using accurate data for a representative bead will ensure a higher degree of accuracy in the prediction of LCTE for the part.

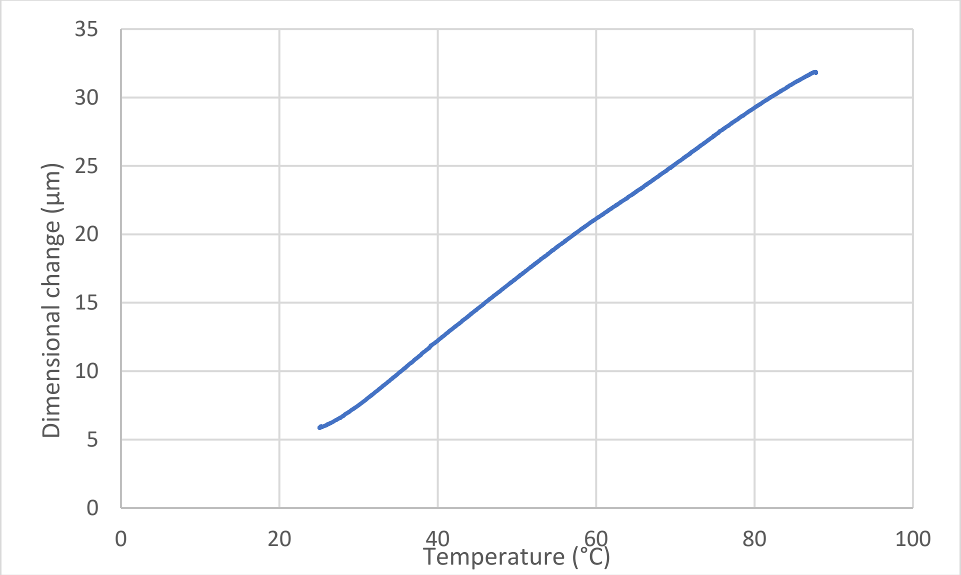

Figure 5. Graph of thermal expansion between 30 °C and 85 °C of sample 1 in the x direction

Table 1. Linear coefficients of thermal expansion measured by TMA

Sample	X-Axis LCTE (µm/m°C)	Y-Axis LCTE (µm/m°C)
1	19.41	46.23
2	15.93	64.87
Average	17.67	55.55

3.2 Application of Laminate Theory

Analogies for comparing short-fiber reinforced composites to laminates are not a new idea. Halpin and Pagano described a method in 1969 of treating randomly oriented short-fiber reinforced composites as laminates by describing them as quasi-isotropic laminates to predict mechanical behavior [24]. Halpin's work, along with others from that time, proved the applicability of using composite laminate theory on other types of composites if an analogy could be made between the two. Parts with simple angled raster patterns produced using AM and continuous fiber laminates have some similarities: the mechanical properties of each is related to the macrostructure of the part or laminate and each have high stiffness regions (continuous fibers in laminates and bead interfaces where fibers are highly aligned). Given these similarities, this study will assess the applicability of using elementary composite laminate theory to predict the LCTE of a cube with raster orientation of 0-90. The theory was not applied to the 0-0 case as it will only return the LCTE used as the material properties since it is a trivial case where all lamina are aligned. To apply laminate theory to the cubes, the following assumptions were applied: each layer in the printed part is analogous to an orthotropic continuous fiber lamina with the same orientation and material properties, stresses in z direction are negligible, the x-direction is the 1-direction, the y-direction is the 2-direction and the thickness dimension is much smaller than the length or width dimensions [25]. Before calculations could start necessary material properties were measured, α_1 (17.7 µm/m°C) and α_2 (55.6 µm/m°C), or obtained from other works, E_1 (8.4 GPa), E_2 (2.7 GPa), ν_{12} (0.37), ν_{21} (0.2) and G_{12} (.9625 GPa) [10, 25, 26].. It is worth noting that the Poisson's ratios and shear modulus were from 15 % weight carbon fiber ABS and the difference could be reflected in the data. The steps for calculating the LCTE of the part as a whole starts with the calculation of the stiffness matrix, [Q], of the lamina, which is based entirely on its material properties. Following this the [A], [B] and [D] matrices, or in physical terms the extensional stiffness matrix, coupling stiffness matrix, and bending stiffness matrix, respectively, are calculated. Next, the [N] matrix, stress resultant matrix, and [M] matrix, moment resultant matrix, were calculated using the LCTE and the relevant temperature range. These, along with matrix manipulation of the [A], [B] and [D] matrices, are used to calculate the LCTE of the laminate. The full process can be seen in Daniel's text [25].When laminate theory was applied to the 0-90 cube, the x-axis and y- axis LCTE were calculated to be 28.39 µm/m°C and 28.39 µm/m°C respectively, which is as one would expect for 0-90 and an even number of layers (24 in this case).

3.3 DIC Results

The DIC results were primarily focused on characterizing the LCTE of the material in the two primary directions (x- and y-axes) and documenting their relationship to the raster orientation of the part. Figure 6 (a-b) shows the averaged strain maps for the x- and y-directions at 90 °C, after low temperature noise had been subtracted, for the 0-0 cube. The strain maps are not meant for comparison between the two but rather to understand local strains on the surface for each direction. In the 90 °C strain map in the x-direction, there is no pattern to the data, however, when looking at the y-direction strain map, there seems to be slight banding of higher and lower strain areas. These bands of high strain align with bead interfaces, this high strain could be due to the high amount of fibers aligned in the x direction near bead interfaces and thus a lack of fibers oriented in the y direction to keep the matrix from expanding in that direction. Some negative strain can be seen in the 90 °C photos, but these are primarily due to edge effects, print defects, and artifacts on the cube.

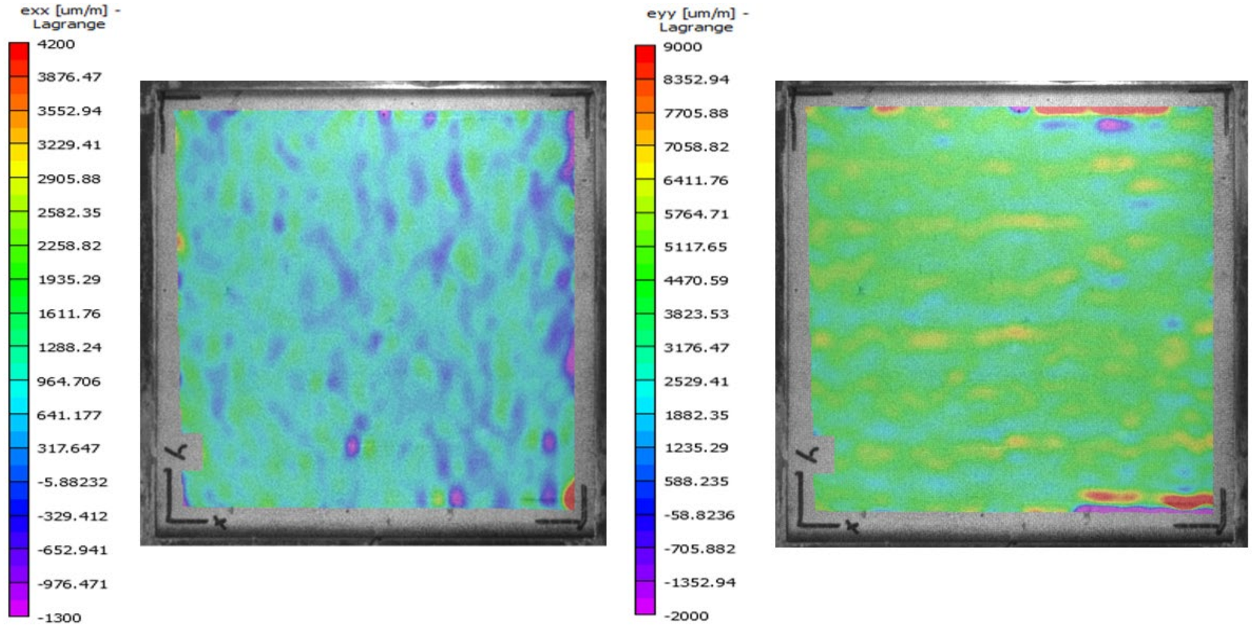

Figure 6. Strain maps of the 0-0 cube at 90 °C (a) x-direction, (b) y-direction

The averaged 90 °C 0-90 cube data can be seen in Figure 7 (a-b). Again, the 20 °C noise has been subtracted from these photos. It is important to remember in the 0-90 cube that the x- and y-axes are arbitrary. Strain in the y-direction, again shows an easily discernable banded structure that overlays the bead interfaces of the cube, where the areas of higher strain match the bead to bead interfaces. The most likely culprit is either the bead to bead interface itself or the fiber orientation differences between the middle and edge of the beads, but there could be other influencing factors. The y-direction strain map at 90 °C shows no pattern or artifacts in the data.

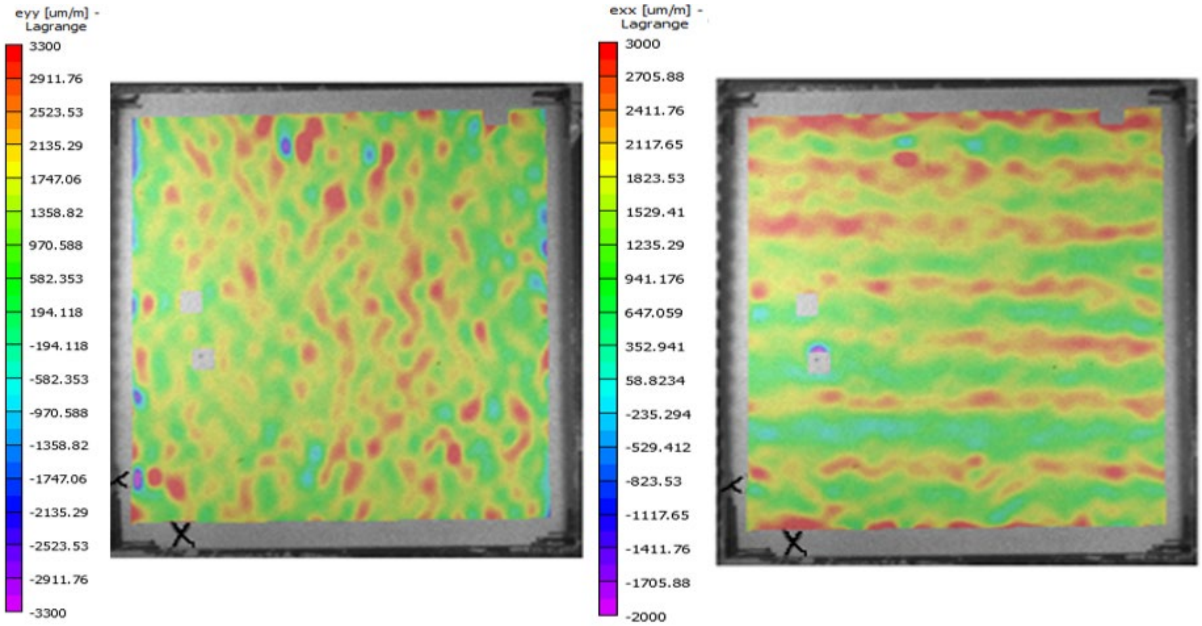

Figure 7. Strain maps of the 0-90 cube at 90 °C (a) x-direction, (b) y-direction

The average noise at 20 °C and strain at 90 °C of each of the images was graphed for both cubes in Figure 8. There is a large disparity between the x and y average strain in the 0-0 cube, which is a result of all the layers in the 0-0 cube expanding in a similar pattern of low expansion in the print direction due to the high orientation of fibers and a higher expansion in the y-direction. A different result is achieved due to these highly aligned fibers in the print direction in the 0-90 cube, as layers in the 0-90 cube are expanding perpendicularly to each other and thus causing a LCTE mismatch with adjacent layers. The strain data was collected for the x-z plane and the y-z plane of each of the cubes, ensuring both the x- and y- directions had strain data collected as both the x'- and y'-direction in the photo, and the two numbers were averaged to reduce biasing from measurement. This data can be seen in Table 2. The x and y LCTE are within 1 % of each other in the 0-90, which is significantly closer than the LCTE in the 0-0 cube. This finding indicates that manipulation of raster orientation could possibly be used to control x and y LCTE of LAEDAM parts.

Figure 8. Graph of average strain measured in each of the ninety photos

Table 2. Calculated linear coefficients of thermal expansion using DIC

Sample	**Strain Direction**	**X-Axis LCTE (µm/m°C)**		**Y-Axis LCTE (µm/m°C)**	
0-0	Exx	12.4	14.4	57.3	57.7
	Eyy	16.3		58.0	
0-90	Exx	23.0	23.7	20.5	23.8
	Eyy	24.4		27.0	

The values for LCTEs calculated using DIC were then compared to the calculated LCTEs from laminate theory, the results of which can be seen in Table 3. When treating the DIC as the true value of the LCTEs, the 0-0 orientation shows a 18.7 % difference in the x LCTE and a 3.7 % difference in the y LCTE. In this case, laminate theory could act as a good estimate for y LCTE in a part, but not for the x LCTE. For the 0-90 orientation both LCTEs show a difference of almost 22 %. This means that, currently, laminate theory would serve as a poor approximation for parts with this configuration. The large difference in the results for the x LCTE in the 0-0 orientation and both LCTEs for the 0-90 orientation may be due to a need for more data points to represent the LCTEs, a need for a different weight function when calculating the average, or a combination of these and other reasons. Using the current process and data, laminate theory does not serve as an accurate prediction of LCTEs of a LAEDAM part.

Table 3. Comparison of laminate theory and DIC LCTE

	Laminate Theory		**DIC**	
	X-Axis LCTE (µm/m°C)	**Y-Axis LCTE (µm/m°C)**	**X-Axis LCTE (µm/m°C)**	**Y-Axis LCTE (µm/m°C)**
0-0	17.7	55.6	14.4	57.7
0-90	28.9	28.9	23.7	23.8

4. CONCLUSIONS

This work investigates the use of DIC to measure strain in a LAEDAM part as well as the applicability of laminate theory combined with measured LCTE from TMA testing. The DIC testing has shown not only an accurate measurement of the strain in the part, but it also showed that print artifacts can be seen in the strain maps. The DIC system this work used can still be further improved to produce even more accurate results going forward. TMA test data are valuable for understanding the variation of LCTE across the bead and can serve as an estimate for a whole part printed with a 0-0 orientation, which was seen in the 0-0 section under laminate theory in Table 3. The laminate theory results will most likely converge toward the DIC data if the bead's LCTE is characterized at more intermediary points. TMA data, even when combined with the laminate theory and chosen assumptions, is only suited for a crude prediction of the LCTE of a part with alternating angled raster orientations. This could be resultant of, again, more in-depth LCTE for the bead, poor assumptions, or due to some inaccurate properties as mentioned before. In reality it is most likely some mixture of all three. The 0-90 cube did show the same behavior in both the DIC and laminate theory, though as expected the LCTE in the x- and y- direction match. Until further investigation into accurately predicting LCTE of a part using TMA data is accomplished, its limitations make DIC the most reliable way to obtain LCTE values of a part.

5. REFERENCES

1. Mieloszyk, J., A. Tarnowski, M. Kowalik, R. Perz, and W. Rzadkowski, *Preliminary design of 3D printed fittings for UAV.* Aircraft Engineering and Aerospace Technology, 2019. https://doi.org/10.1108/AEAT-07-2018-0182
2. Kasparova, M., L. Grafova, P. Dvorak, T. Dostalova, A. Prochazka, H. Eliasova, J. Prusa, and S. Kakawand, *Possibility of reconstruction of dental plaster cast from 3D digital study models.* BioMedical Engineering OnLine, 2013. **12**(1): p. 49. https://doi.org/10.1186/1475-925x-12-49
3. Skowyra, J., K. Pietrzak, and M.A. Alhnan, *Fabrication of extended-release patient-tailored prednisolone tablets via fused deposition modelling (FDM) 3D printing.* European Journal of Pharmaceutical Sciences, 2015. **68**: p. 11-17. https://doi.org/10.1016/j.ejps.2014.11.009
4. Hassen, A.A., R. Springfield, J. Lindahl, B. Post, L. Love, C. Duty, U. Vaidya, R.B. Pipes, and V. Kunc. *The durability of large-scale additive manufacturing composite molds*. in Composites and Advanced Materials Expo (CAMX) Conference. 2016.

5. Hassen, A.A., J. Lindahl, X. Chen, B. Post, L. Love, and V. Kunc. *Additive manufacturing of composite tooling using high temperature thermoplastic materials*. in SAMPE Conference Proceedings, Long Beach, CA, May. 2016.
6. Kunc, V., J. Lindah, R.B. Dinwiddie, B.K. Post, L.J. Love, C. Duty, M. Matlack, R. Fahey Jr, and A.A. Hassen. *Investigation of In-autoclave Additive Manufacturing Composite Tooling*. in CAMX Conference, Anaheim, CA. 2016.
7. Sudbury, T.Z., R. Springfield, V. Kunc, and C. Duty, *An assessment of additive manufactured molds for hand-laid fiber reinforced composites.* The International Journal of Advanced Manufacturing Technology, 2017. **90**(5): p. 1659-1664. https://doi.org/10.1007/s00170-016-9464-9
8. Masood, S. and W. Song, *Development of new metal/polymer materials for rapid tooling using fused deposition modelling.* Materials & design, 2004. **25**(7): p. 587-594.
9. Twigg, G., A. Poursartip, and G. Fernlund, *Tool–part interaction in composites processing. Part I: experimental investigation and analytical model.* Composites Part A: Applied Science and Manufacturing, 2004. **35**(1): p. 121-133. https://doi.org/10.1016/S1359-835X(03)00131-3
10. Hill, C., K. Rowe, R. Bedsole, J. Earle, and V. Kunc, *Materials and Process Development for Direct Digital Manufacturing of Vehicles*. 2016.
11. Sung-Hoon, A., M. Michael, O. Dan, R. Shad, and K.W. Paul, *Anisotropic material properties of fused deposition modeling ABS.* Rapid Prototyping Journal, 2002. **8**(4): p. 248-257. https://doi.org/10.1108/13552540210441166
12. Zaldivar, R.J., D.B. Witkin, T. McLouth, D.N. Patel, K. Schmitt, and J.P. Nokes, *Influence of processing and orientation print effects on the mechanical and thermal behavior of 3D-Printed ULTEM® 9085 Material.* Additive Manufacturing, 2017. **13**: p. 71-80. https://doi.org/10.1016/j.addma.2016.11.007
13. Velez-Garcia, G., A. Wright, V. Kunc, and C. Duty, *Coefficient of Thermal Expanstion Test Report.* ORNL Technical Report, 2014. **ORNL/TM-2014/334**.
14. Love, L.J., V. Kunc, O. Rios, C.E. Duty, A.M. Elliott, B.K. Post, R.J. Smith, and C.A. Blue, *The importance of carbon fiber to polymer additive manufacturing.* Journal of Materials Research, 2014. **29**(17): p. 1893-1898. https://doi.org/10.1557/jmr.2014.212
15. Duty, C.E., T. Drye, and A. Franc, *Material Development for Tooling Applications Using Big Area Additive Manufacturing (BAAM)*. 2015, ; Oak Ridge National Lab. (ORNL), Oak Ridge, TN (United States). Manufacturing Demonstration Facility (MDF). p. Medium: ED.
16. Lhotellier, F.C. and H.F. Brinson, *Matrix-fiber stress transfer in composite materials: Elasto-plastic model with an interphase layer.* Composite Structures, 1988. **10**(4): p. 281-301. https://doi.org/10.1016/0263-8223(88)90007-4
17. Advani, S.G. and C.L.T. III, *The Use of Tensors to Describe and Predict Fiber Orientation in Short Fiber Composites.* Journal of Rheology, 1987. **31**(8): p. 751-784. https://doi.org/10.1122/1.549945
18. Affdl, J.C.H. and J.L. Kardos, *The Halpin-Tsai equations: A review.* Polymer Engineering & Science, 1976. **16**(5): p. 344-352. https://doi.org/10.1002/pen.760160512
19. E. Verweyst, B. and C. Tucker, *Fiber Suspensions in Complex Geometries: Flow/Orientation Coupling*. Vol. 80. 2002. 1093-1106.
20. Tekinalp, H.L., V. Kunc, G.M. Velez-Garcia, C.E. Duty, L.J. Love, A.K. Naskar, C.A. Blue, and S. Ozcan, *Highly oriented carbon fiber–polymer composites via additive*

manufacturing. Composites Science and Technology, 2014. **105**: p. 144-150. https://doi.org/10.1016/j.compscitech.2014.10.009

21. Laboratory, O.R.N., *Manufacturing Demonstration Facility Annual Report: Polymer Additive Manufacturing*, D.o. Energy, Editor. 2014: Oak Ridge, TN.
22. *ASTM E831-14, Standard Test Method for Linear Thermal Expansion of Solid Materials by Thermomechanical Analysis*. 2019, ASTM International, West Conshohocken, PA, 2014.
23. Pan, B., K. Qian, H. Xie, and A. Asundi, *Two-dimensional digital image correlation for in-plane displacement and strain measurement: a review*. Measurement Science and Technology, 2009. **20**(6): p. 062001. https://doi.org/10.1088/0957-0233/20/6/062001
24. Halpin, J.C. and N.J. Pagano, *The Laminate Approximation for Randomly Oriented Fibrous Composites*. Journal of Composite Materials, 1969. **3**(4): p. 720-724. https://doi.org/10.1177/002199836900300416
25. Daniel, I.M. and O. Ishai, *Engineering mechanics of composite materials*. 2nd ed. 2006, New York: Oxford University Press. xviii, 411 p.
26. Zhang, W., C. Cotton, J. Sun, D. Heider, B. Gu, B. Sun, and T.-W. Chou, *Interfacial bonding strength of short carbon fiber/acrylonitrile-butadiene-styrene composites fabricated by fused deposition modeling*. Composites Part B: Engineering, 2018. **137**: p. 51-59. https://doi.org/10.1016/j.compositesb.2017.11.018